A Spectral Simple Adjoint Method for Retrieving Low-Altitude Winds from Single-Doppler Data

CHONG-JIAN QIU AND QIN XU

Cooperative Institute for Mesoscale Meteorological Studies, University of Oklahoma/NOAA, Norman, Oklahoma

(Manuscript received 28 June 1993, in final form 7 January 1994)

ABSTRACT

A spectral simple adjoint (SSA) method for retrieving low-altitude time-mean horizontal winds from single-Doppler wind measurements is developed and tested with the Phoenix II field experimental data. The SSA method is similar to the previous grid simple adjoint (GSA) methods of Qiu and Xu and Xu et al., except that a truncated spectral expression is used to replace the grid representation of the wind field. In the previous GSA methods the retrieved time-mean winds were resolved on the same full spatial grid as the data. This full spatial resolution was often excessive and unnecessary as the time-mean wind field was quite smooth. When a truncated spectral expression is used to reduce the excessive and unnecessary spatial resolution, the SSA method not only gains temporal resolution (e.g., the retrieving period can be reduced to 130 s—a single time interval of radar scan) but also improves the accuracy of the retrieved winds (because short-wave noise is filtered). The merits and limitations of the SSA method are also examined with idealized examples.

1. Introduction

The grid simple adjoint (GSA) method of Qiu and Xu (1992, henceforth referred to as QX92) has been recently upgraded and tested by Xu et al. (1994a,b, henceforth referred to as XQY94a,b) with the Phoenix II field experiment data (Schneider and Lilly 1986) for retrieving the low-altitude time-mean winds from single-Doppler reflectivity and/or radial wind. The results showed that using a sequence of observational data over several time levels of radar scans not only increased the accuracy of the retrieval but also made the method less sensitive to data errors and temporal wind fluctuations. In particular, as shown in XQY94b, the time-mean wind field (averaged over three time intervals: 3×130 s) retrieved from the single-Doppler radial wind data was quite close to the dual-Doppler observed wind field, while rms error was 1.19 m s^{-1}. In principle, if the time-mean wind field is retrieved on the same spatial grid as the data, the retrieved wind field can have the same high spatial resolution as the data. In practice, however, this high spatial resolution may be excessive and unnecessary if the time-mean wind field is smooth. This was probably the case in the Phoenix II data. In particular, as shown in XQY94a,b, the time-mean wind fields retrieved over many time levels of radar scans were quite smooth, so the high spatial resolution used in the GSA methods seemed excessive and unnecessary. Also, as many time levels were used to retrieve the time-mean fields, the retrieved fields had relatively low temporal resolution. This loss of temporal resolution could be the price paid for the excessive and unnecessary spatial resolution. Thus, it is possible and desirable to further improve the GSA methods by reducing the spatial resolution of the retrieved wind field (but not the resolution of the data field) and gaining some temporal resolution. This is the motivation of this study.

To achieve the aforementioned objective, a spectral simple adjoint (SSA) method is developed in this paper. This method is similar to the previous GSA method of XQY94b, except that a truncated spectral expression is used to replace the grid representation of the wind field. In terms of using truncated spectral expressions, the method is similar to the S2 scheme in Xu and Qiu (1994, henceforth referred to as XQ94). But, the truncated spectral expression in XQ94 was for the streamfunction on a surface normal to the radar beam in the reflectivity equation and the S2 scheme was tested only with artificial reflectivity data. In this paper the truncated spectral expression is used for the horizontal wind field in the radial momentum equation and the SSA method will be tested with the radial wind data measured during the Phoenix II field experiment. As we will see in this paper, using truncated spectral expressions for the retrieved fields may not only allow a relatively high temporal resolution (e.g., the retrieving period can reduce even to 130 s—a single time interval of radar scan) but also directly improve the accuracy of the retrievals (because short-wave noise is largely filtered by the spectral truncation). The SSA method

Corresponding author address: Prof. Qin Xu, CIMMS, University of Oklahoma, 100 East Boyd St., Room 1110, Norman, OK 73019-0628.

and adjoint formulation are described in the next section. The results of experiments with the Phoenix II data are presented in section 3. The merits and limitations of the SSA method are discussed in section 4. Conclusions follow in section 5.

2. Method and adjoint formulation

In cylindrical coordinates (r, α, z) centered on a single-Doppler radar, the radial momentum equation has the following form:

$$\partial_t v_r + v_r \partial_r v_r + \left(\frac{v_\alpha}{r}\right)\partial_\alpha v_r - \frac{v_\alpha^2}{r} + w\partial_z v_r + \left(\frac{1}{\rho}\right)\partial_r p = \kappa \nabla_H^2 v_r + \nu \partial_z^2 v_r, \quad (2.1)$$

where $\mathbf{v} \equiv (v_r, v_\alpha)$ is the horizontal wind vector, v_r is the radial component, v_α is the tangential component, w is the vertical velocity, p is the pressure, ρ is the density, ∇_H^2 is the horizontal Laplacian in the cylindrical coordinates, κ is the coefficient of horizontal eddy viscosity, ν is the coefficient of vertical eddy viscosity, and the coordinate-related viscous term $-\kappa(v_r + 2\partial_\alpha v_\alpha)/r^2$ (see Batchelor 1967, 602–603) is neglected since the data field was not very close to the radar as shown in Fig. 1 of XQY94a.

For a selected retrieving period τ (which covers several sequential radar scans), the horizontal wind can be partitioned into a time-mean part, $\mathbf{v}_m \equiv (v_{rm}, v_{\alpha m})$, and a temporal fluctuation part, $\mathbf{v}' \equiv (v_r', v_\alpha')$, where $(\,)_m \equiv \tau^{-1}\int_0^\tau (\,)dt$. Substituting $\mathbf{v} = \mathbf{v}_m + \mathbf{v}'$ into (2.1) (but with v_r retained as a "tracer" field) gives

$$\partial_t v_r + v_{rm}\partial_r v_r + \left(\frac{v_{\alpha m}}{r}\right)\partial_\alpha v_r - \frac{v_{\alpha m}^2}{r} - \kappa \nabla_H^2 v_r = F \approx F_m, \quad (2.2)$$

where the forcing term F is the sum of all the remaining terms and F_m is the time-mean part of the forcing F. As shown in XQY94b, the unknown temporal fluctuation part of the forcing F can be neglected if the retrieving period is relatively short. As explained in Xu et al. (1992) and XQY94b, although the unknown temporal fluctuation part of the forcing F cannot be retrieved, the time-mean part of the unknown forcing can be retrieved, so F_m is retained in (2.2). The coefficient of horizontal eddy viscosity κ is assumed as an unknown constant and also can be retrieved.

Using (2.2) as the governing equation, we need to retrieve $(\mathbf{v}_m, F_m, \kappa)$ from single-Doppler observations of v_r. The objective is to find the best time-mean estimate of $(\mathbf{v}_m, \kappa, F_m)$ over a period τ that gives the best "prediction" of v_r in terms of minimizing the following cost function:

$$J \equiv \int_0^\tau \iint_\Omega (P_1\Delta^2 + P_2\Delta_m^2 + P_3\epsilon^2)\,d\Omega dt = J_1 + J_2 + J_3, \quad (2.3)$$

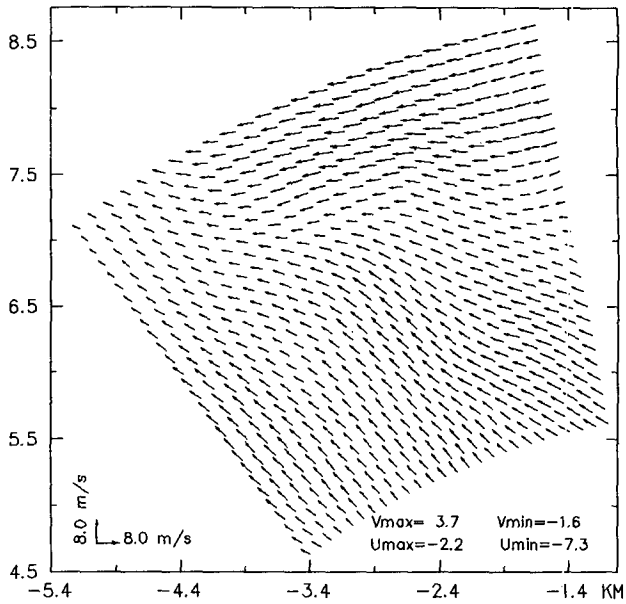

FIG. 1. Observed time-mean winds averaged over the four time levels in dataset A.

where the integral is over $\Omega \times [0, \tau]$; P_1 and P_2 are nondimensional weights, $\Delta \equiv v_r - v_{\text{rob}}$, $\Delta_m \equiv v_{rm} - v_{rm\text{ob}}$, where the subscript ob represents the observed value; P_3 (m^2) is a dimensional weight; $\epsilon \equiv \nabla_H \cdot \mathbf{v}_m$ is the horizontal divergence of $\mathbf{v}_m$ in the cylindrical coordinates, where $\mathbf{v}_m$ is the estimated time-mean horizontal wind; and Ω is the selected region for retrieval (which is the same as in Fig. 1 of XQY94a). The values for P_1, P_2, and P_3 are listed in section 3b, which are the same as in X94b. Here, v_r is "predicted" from the governing equation (2.2) with estimated $(\mathbf{v}_m, \kappa, F_m)$ and the following boundary and initial conditions:

$$v_r(t, x, y) = v_{\text{rob}}(t, x, y) \quad \text{at the boundary of domain } \Omega, \quad (2.4)$$

$$v_r(0, x, y) = v_{\text{rob}}(0, x, y). \quad (2.5)$$

The second part, J_2, of the cost function in (2.3) gives only a weak constraint on the difference between v_{rm} and $v_{rm\text{ob}}$ (Sasaki 1970). As explained in XQY94b, this weak constraint is better than the strong constraint that requires $\Delta_m = 0$ or $v_{rm} = v_{rm\text{ob}}$, because allowing a small difference Δ_m reduces the error in the estimated $v_{\alpha m}$ significantly. It is not necessary to require $v_{rm} = v_{rm\text{ob}}$, since $v_{rm\text{ob}}$ contains observational error. The last part, J_3, of the cost function imposes a weak nondivergence constraint on the retrieved horizontal wind field. With a proper weight P_3, this weak constraint can improve the retrieval, even for microburst winds characterized by strong divergence (see Xu et al. 1993).

A complete spectral expansion of a discrete field over a limited domain can be done in two ways. The first way is to extend the field to a larger and periodic do-

main and then apply discrete Fourier transformation. The second way is to separate the field into a harmonic part satisfying the nonhomogeneous boundary condition and a nonharmonic part satisfying the homogeneous boundary condition, then apply discrete Fourier transformation to the nonharmonic part (Chen and Kuo 1992). The first way is straightforward and simple, but may be computationally less efficient as the Fourier transformation is made over the extended domain. The second way may be computationally efficient, but complex and applicable only for a regular domain. Since we are only interested in truncated spectral expansions (instead of complete spectral expansions), it is relatively easy to consider a truncation based on the first method of complete spectral expansion. In this case, $(\varphi^1, \varphi^2, \varphi^3) \equiv (v_{rm}, v_{\alpha m}, F_m)$ can be expressed by the following truncated spectral expansions:

$$\varphi^i = \sum\sum \left[A^i_{n,l} \cos\left(\frac{n\pi\alpha}{\Phi_2}\right) \cos\left(\frac{l\pi r}{R_2}\right) + B^i_{n,l} \sin\left(\frac{n\pi\alpha}{\Phi_2}\right) \cos\left(\frac{l\pi r}{R_2}\right) + C^i_{n,l} \cos\left(\frac{n\pi\alpha}{\Phi_2}\right) \sin\left(\frac{l\pi r}{R_2}\right) + D^i_{n,l} \sin\left(\frac{n\pi\alpha}{\Phi_2}\right) \sin\left(\frac{l\pi r}{R_2}\right) \right], \quad (2.6)$$

where the double summations are for n (from 0 to 9) and l (from 0 to 9); $R_2 = 4R_0$, $\Phi_2 = 360° = 14.4\Phi_0$, $R_0 \times \Phi_0 = (27 \times 112 \text{ m}) \times (25 \times 1°)$ is the domain Ω specified in (2.3) (also see Fig. 1) and $R_2 \times \Phi_2$ is the extended (periodic) domain in the aforementioned first way of complete spectral expansions; and $A^i_{n,l}$, $B^i_{n,l}$, $C^i_{n,l}$, and $D^i_{n,l}$ (with $i = 1, 2, 3$) are the unknown spectral coefficients that need to be retrieved. As explained above, the long-wave components (with r wavelength longer than R_0, or α wavelength longer than Φ_0) in (2.6) are required by the nonhomogeneous boundary condition.

Since the spectral adjoint method used in this paper is not the same as the previously developed adjoint for spectral prognostic equations (such as Navon et al. 1992), we need to show the adjoint formulation and to derive the gradient of the cost function J with respect to the spectral coefficients and eddy coefficient κ. First, the leading-order variation of (2.2), and (2.4) and (2.5) can be obtained as follows:

$$\partial_t \delta v_r + v_{rm}\partial_r \delta v_r + \left(\frac{v_{\alpha m}}{r}\right)\partial_\alpha \delta v_r - \kappa\nabla_H^2 \delta v_r = \delta F_m - (\partial_r v_r)\delta v_{rm} - \frac{1}{r}(\partial_\alpha v_r - 2v_{\alpha m})\delta v_{\alpha m} + (\nabla_H^2 v_r)\delta\kappa, \quad (2.7a)$$

$$\delta v_r(t, x, y) = 0 \quad \text{at the boundary of domain } \Omega, \quad (2.7b)$$

$$\delta v_r(0, x, y) = 0. \quad (2.7c)$$

Then, the associated adjoint problem for v^* is given by

$$\delta_t v^* + \frac{1}{r}[\partial_r(r v_{rm} v^*) + \partial_\alpha(v_{\alpha m} v^*)] + \kappa\nabla_H^2 v^* = 2P_1\Delta, \quad (2.8a)$$

$$v^*(t, x, y) = 0 \quad \text{at the boundary of domain } \Omega, \quad (2.8b)$$

$$v^*(\tau, x, y) = 0, \quad (2.8c)$$

where P_1 and Δ are defined in (2.3). By integrating v^*(2.7a) + δv_r(2.8a) over $\Omega \times [0, \tau]$ and using the boundary and initial conditions (2.7b) and (2.7c), and (2.8b) and (2.8c), we obtain a formulation for the variation of J_1; that is,

$$\int_0^\tau \int\int_\Omega \left[(v^*\partial_r \delta v_r)\delta v_{rm} + \frac{v^*}{r}(\partial_\alpha v_r - 2v_{\alpha m}) \times \delta v_{\alpha m} - v^*\delta F_m - (v^*\nabla_H^2 v_r)\delta\kappa \right] d\Omega dt = \int_0^\tau \int\int_\Omega (2P_1\Delta)\delta v_r d\Omega dt \equiv \delta J_1. \quad (2.9a)$$

It is easy to verify that the variations of J_2 and J_3 are

$$\delta J_2 = \int_0^\tau \int\int_\Omega 2P_2\Delta_m \delta v_{rm} d\Omega dt, \quad (2.9b)$$

$$\delta J_3 = \int_0^\tau \int\int_\Omega 2P_3\epsilon\nabla_H \cdot \delta \mathbf{v}_m d\Omega dt. \quad (2.9c)$$

Note that only the retrieved variables $(v_{rm}, v_{\alpha m}, F_m)$ are expressed by the truncated spectral expansions (2.6), while the predicted variables δv_r in (2.7a)–(2.7c) and v^* in (2.8a)–(2.8c) are still expressed on the same grid as the observed variable v_r. The variations in (2.7)–(2.9) are made with respect to the spectral components of $(v_{rm}, v_{\alpha m}, F_m)$ and to the grid values of v_r and v^*. Substituting δ(2.6) into (2.9a) + (2.9b) + (2.9c) gives

$$\delta J = \sum\sum\sum \left[\left(\frac{\partial J}{\partial A^i_{n,l}}\right)\delta A^i_{n,l} + \left(\frac{\partial J}{\partial B^i_{n,l}}\right)\delta B^i_{n,l} + \left(\frac{\partial J}{\partial C^i_{n,l}}\right)\delta C^i_{n,l} + \left(\frac{\partial J}{\partial D^i_{n,l}}\right)\delta D^i_{n,l} \right] + \left(\frac{\partial J}{\partial \kappa}\right)\delta\kappa, \quad (2.10)$$

where the triple summations are for j (from 1 to 3), n (from 0 to 9), and l (from 0 to 9). Here, $\partial J/\partial A^i_{n,l}$ is the gradient of J with respect to $A^i_{n,l}$ and its three components (corresponding to $i = 1, 2, 3$) are given by

$$\frac{\partial J}{\partial A^1_{n,l}} = \int\int_\Omega \left\{\left[\int_0^\tau v^* \partial_r v_r dt + 2\tau\left(P_2\Delta_m + \frac{P_3\epsilon}{r}\right)\right]\cos\left(\frac{n\pi\alpha}{\Phi_2}\right)\cos\left(\frac{l\pi r}{R_2}\right) - (2\tau P_3\epsilon)\left(\frac{l\pi}{R_2}\right)\cos\left(\frac{n\pi\alpha}{\Phi_2}\right)\sin\left(\frac{l\pi r}{R_2}\right)\right\} d\Omega,$$

$$\frac{\partial J}{\partial A^2_{n,l}} = \int\int_\Omega \left[\frac{1}{r}\left(\int_0^\tau v^* \partial_\alpha v_r dt - 2\tau v_{\alpha m}\right)\cos\left(\frac{n\pi\alpha}{\Phi_2}\right)\cos\left(\frac{l\pi r}{R_2}\right) - \left(\frac{2\tau P_3\epsilon}{r}\right)\left(\frac{n\pi}{\Phi_2}\right)\sin\left(\frac{n\pi\alpha}{\Phi_2}\right)\cos\left(\frac{l\pi r}{R_2}\right)\right] d\Omega,$$

$$\frac{\partial J}{\partial A^3_{n,l}} = \int\int_\Omega \left[\left(\int_0^\tau v^* dt\right)\cos\left(\frac{n\pi\alpha}{\Phi_2}\right)\cos\left(\frac{l\pi r}{R_2}\right)\right] d\Omega, \qquad (2.11)$$

where the two weights P_2 and P_3 are assumed constant. The components of gradients $\partial J/\partial B^i_{n,l}$, $\partial J/\partial C^i_{n,l}$, and $\partial J/\partial D^i_{n,l}$ are similar to those in (2.11) and the detailed formulations are omitted here. The gradient of J with respect to κ is given by

$$\frac{\partial J}{\partial \kappa} = \int\int_\Omega \left(\int_0^\tau v^* \nabla_H^2 v_r dt\right) d\Omega. \qquad (2.12)$$

The retrieving procedures consist of the following iterative steps with zero initial guesses for the spectral coefficients and κ: (i) Compute the grid values of (v_{rm}, $v_{\alpha m}$, F_m) from (2.6). (ii) Integrate (2.7a)–(2.7c) forward and integrate (2.8a)–(2.8c) backward in time by using the finite-difference scheme. (iii) Compute the gradient components from (2.11) and (2.12) etc. (iv) Find the local minimum of J along the direction of the gradient (i.e., the direction of the steepest descent of J) and, thus, obtain new estimates of spectral coefficients and κ. (v) Go back to step (i) and repeat the above procedure until J reaches the global minimum. As in QX92 and XQY94b, the standard algorithm (UMCGG in the IMSL math library) is used for finding the local minimum of J. The numerical code is designed carefully to ensure the conjugate property between the discretized operator and adjoint operator. The detailed process of finding the discrete adjoint from a discrete model can be found in Talagrand and Courtier (1987) and Thacker and Long (1988).

3. Experiments and test results

a. Phoenix II data

The Phoenix II data collected by the two National Oceanic and Atmospheric Administration (NOAA) X-band Doppler radars (i.e., radar C and radar D as shown in Fig. 1 of XQY94a) on 17 and 22 June 1984 are selected for testing. As in XQY94a,b, the raw dual-Doppler data are interpolated from the lowest three elevation angles (0.594°, 1.484°, 2.484°) to the level of $z = 196$ m over the horizontal area of 5769 m $\leq r \leq$ 5769 m + 27Δr and 324° $\leq \alpha \leq$ 324° + 25$\Delta\alpha$. Here, (Δr, $\Delta\alpha$) = (112 m, 1°) are the grid resolutions in the cylindrical coordinates (centered at radar C). Since the time elapsed for scanning through the lowest three elevation angles is much shorter (13–14 s) than the time interval for the entire volume scan (about 130 s), the data measured by one scan through the lowest three elevation angles are considered approximately as one-time-level data. In this way, the following four sets of grided data are prepared and each dataset contains four time levels of observations:

set A covers the period of 1437:26–1443:58 LST 22 June 1984;

set B covers the period of 1318:32–1324:48 LST 22 June 1984;

set C covers the period of 1237:28–1243:58 LST 17 June 1984;

set D covers the period of 1633:32–1639:03 LST 22 June 1984.

When the radial wind field is used as a scalar field for the adjoint method, it is necessary to filter the radar noise from the raw data with a relatively large nondimensional Cressman radius [$R = 7$, where $R^2 \equiv (r_{\text{raw}} - r_{\text{grid}})^2/\Delta r^2 + (\alpha_{\text{raw}} - \alpha_{\text{grid}})^2/\Delta\alpha^2$, ($r_{\text{raw}}$, α_{raw}) is the raw data point, and (r_{grid}, α_{grid}) is the grid point in the cylindrical coordinates]. This situation and treatment are the same as in XQY94b. Examples of filtered radial wind fields are shown in Fig. 1 of XQY94b. However, when the dual-Doppler wind data are used to obtain the observed time-mean wind field (Fig. 1), a relatively small nondimensional Cressman radius ($R = 2$) is used to retain as much as possible the spatial resolution while radar noise is partially filtered by time averaging.

b. Experimental design

To test the merits of the SSA method, four groups of experiments are designed and compared with the results obtained by the previous GSA method of XQY94b. The first group of experiments (A1–D1) uses four time levels of data and the retrieving period covers three time intervals of observations; that is, $\tau \equiv N\Delta\tau = 3 \times 130$ s. The computational time step is $\Delta t = 6.5$ s and the radial wind data are interpolated with the cubic-spline scheme to each computational time level and used in the backward time integration of the

TABLE 1. Root-mean-square error (m s^{-1}) (relative rms error in percent) of the retrieved winds in experiment 1 (with $N = 3$).

Dataset	GSA	SSA	Truncation
A	1.47 (31.7%)	0.86 (18.5%)	0.38 (8.1%)
B	1.01 (28.4%)	0.98 (27.7%)	0.30 (8.4%)
C	1.38 (29.3%)	1.03 (21.7%)	0.63 (13.4%)
D	0.95 (17.5%)	0.76 (13.4%)	0.31 (5.6%)
Average	1.20 (26.7%)	0.90 (20.3%)	0.41 (8.9%)

TABLE 2. Root-mean-square error (m s^{-1}) (relative rms error in percent) of the retrieved winds in experiment 2 (with $N = 3$ and $P_2 = 0$).

Dataset	GSA	SSA
A	2.36 (50.9%)	1.60 (34.6%)
B	1.93 (54.5%)	1.15 (32.4%)
C	3.41 (72.1%)	2.00 (42.2%)
D	1.69 (31.1%)	1.10 (20.3%)
Average	2.34 (52.9%)	1.46 (32.3%)

adjoint equation (2.8). As in XQY94a,b, this cubic-spline interpolation improves the retrieval, in addition to the aforementioned Cressman filtering of the raw data and the following proper specifications of weights:

$$P_1 = \left(\frac{\tau}{t + \Delta t}\right)^{1/2},$$

$$P_2 = 0.01 P_{1m} \quad \text{with} \quad P_{1m} \equiv \frac{1}{\tau}\int_0^{\tau} P_1 dt,$$

$$P_3 = k\sigma_v^2 P_{1m} \quad \text{with} \quad k = 500 \text{ m}^2,$$

where σ_v is the amplitude of v_r (estimated by the rms of the spatial variation of v_r at $t = 0$). These choices of weights are the same as in XQY94b and detailed explanations are given in QX92 and XQY94a,b.

The second group of experiments (A2–D2) is the same as the first group, except that $P_2 = 0$ or, say, the weak constraint imposed on the difference between the retrieved and observed time-mean radial winds is released. In this way, the time-mean horizontal winds are obtained "purely" by the retrieving technique itself in which the radial wind field is treated as a (quasi-conserved) "tracer field" only. This simulates the situation when the three-dimensional winds are retrieved on each surface normal to the radar beams as in QX92 and XQ94. The third group of experiments (A3–D3) is the same as the first group, except that the retrieving period covers only a single time interval of observation; that is, $N = 1$ or $\tau \equiv \Delta\tau = 130$ s. The last group of experiments (A4–D4) sets both $P_2 = 0$ and $N = 1$. All the experiments use 80 iterations of minimization algorithm.

c. Results

For the first group of experiments (A1–D1), the results are summarized in Table 1, where

$$\text{rms}(|\Delta \mathbf{v}_m|) \equiv \left[\frac{\sum |(v_{rm} - v_{rmob}, v_{\alpha m} - v_{\alpha mob})|^2}{(28 \times 26)}\right]^{1/2} \tag{3.1}$$

is the rms error of the retrieved time-mean wind field and the values in parentheses are the relative rms errors with respect to $[\sum |\mathbf{v}_{mob}|^2/(28 \times 26)]^{1/2}$. Here, the summation is over the total number of 28×26 grid points. The last column of Table 1 lists the rms error purely due to the spectral truncation of (2.6), which is computed by the same formulas as (3.1) except that $(v_{rm}, v_{\alpha m})$ are not the retrieved winds but obtained directly by least-squares fitting (2.6) with $(v_{rmob}, v_{\alpha mob})$. The averaged relative rms errors are 26.7%, 20.3%, and 8.9% for the GSA method, SSA method, and spectral truncation, respectively. Clearly, the SSA method improves the retrieval significantly, though about one-half of the error for the SSA method is purely due to the spectral truncation of (2.6).

The results for the second group of experiments (A2–D2) are summarized in Table 2. In this case, the weak constraint imposed on the difference between the retrieved and observed time-mean radial winds is released, so the superior performance of the SSA method is seen more clearly, although both methods become less accurate than in experiments A1–D1.

The results for the third group of experiments (A3–D3) are summarized in Table 3. The retrieved wind fields by the two methods in experiment A3 are shown in Figs. 2a,b and the observed wind is shown in Fig. 1. Clearly, as the retrieving period reduces to a single time interval of observation ($\tau \equiv \Delta\tau = 130$ s), the GSA method gives a poor retrieval (Fig. 2a), while the SSA method still gives a quite accurate retrieval (Fig. 2b). Here, the SSA method (with $N = 1$) seems to be able to retrieve the wind field with the same high temporal resolution as the radar scan.

The results for the fourth group of experiments (A4–D4) are summarized in Table 4. In this case, the superior performance of the SSA method is seen most clearly, although both methods become less accurate than in the above three groups of experiments. The retrieved wind fields in experiment A4 are shown in Figs. 3a,b. Clearly, the GSA method gives a very poor

TABLE 3. Root-mean-square error (m s^{-1}) (relative rms error in percent) of the retrieved winds in experiment 2 (with $N = 1$).

Dataset	GSA	SSA	Truncation
A	2.64 (56.3%)	1.23 (26.2%)	0.56 (11.9%)
B	2.18 (59.8%)	1.11 (30.5%)	0.55 (15.1%)
C	2.95 (62.7%)	1.11 (23.5%)	0.78 (16.7%)
D	2.99 (57.0%)	1.21 (23.1%)	0.43 (8.1%)
Average	2.69 (59.0%)	1.17 (25.8%)	0.58 (13.0%)

retrieval (Fig. 3a), while the SSA method still can give an acceptable retrieval (Fig. 3b).

4. Merits and limitations of the SSA method

The above test results show that when the excessive spatial resolution is reduced by a truncated spectral expression of the retrieval field, the SSA method gains accuracy and/or temporal resolution for the retrieval. This improvement could be related to the fact that both the true and retrieved time-mean wind fields were quite smooth in the Phoenix II case and, thus, the high spatial resolution used in the GSA method was unnecessary. It is also likely that the SSA method may lose its advantage when the wind field is not so smooth and needs to be resolved by nearly the same high spatial resolution as the data. To illustrate the latter problem and understand the merits and limitations of the SSA method, idealized one-dimensional examples are designed and examined as follows.

The first example is similar to that in Figs. 1 and 2 of QX92, except that the first half wavelength of the initial sinusoidal tracer field η [equivalent to v_r in (2.5)] is modified into a "plateau" shape as shown in Fig. 4. The reduced one-dimensional advection equation and boundary and initial conditions are

$$\partial_t \eta + u\partial_x \eta = 0, \quad \text{for} \quad 0 \leqslant t \leqslant \tau, \quad 0 \leqslant x \leqslant 1, \tag{4.1}$$

$$\eta(t, x) = \eta_{ob}(t, x) \quad \text{at} \quad x = 0 \quad \text{and} \quad x = 1, \tag{4.2}$$

$$\eta(0, x) = \eta_{ob}(0, x). \tag{4.3}$$

The "true" velocity field u is assumed to contain only a long-wave mode, that is,

TABLE 4. Root-mean-square error (m s^{-1}) (relative rms error in percent) of the retrieved winds in experiment 2 (with $N = 1$ and $P_2 = 0$).

Dataset	GSA	SSA
A	3.41 (72.5%)	1.91 (40.7%)
B	2.79 (76.4%)	1.53 (41.9%)
C	3.96 (84.3%)	2.30 (49.0%)
D	3.60 (68.7%)	1.55 (29.6%)
Average	3.44 (75.5%)	1.82 (40.3%)

$$u = \sin(2\pi x). \tag{4.4}$$

The "observed" tracer field η_{ob} is generated by integrating (4.1) forward in time from 0 to τ, with grid length $\Delta x = 1/20$ and time step $\Delta t = \Delta\tau \equiv \tau/N = 0.1$ (all nondimensional). The boundary condition is periodic. The initial tracer field $\eta_{ob}(0, x)$ and final tracer field $\eta_{ob}(\tau, x)$ are shown in Fig. 4. The above artificially generated data are used to examine the GSA and SSA methods. The GSA method uses the full 20 grid points to resolve the retrieved u field, while the SSA method uses the following truncated expansion:

$$u = \sum_{n=1}^{M} [A_n \cos(2n\pi x) + B_n \sin(2n\pi x)], \tag{4.5}$$

where the summation is up to M (=5). As shown in Fig. 5, the SSA method gives a nearly perfect retrieval (cf. circles with solid line), but the GSA method completely fails to retrieve the advection velocity u at the three middle grid points over the "plateau" in Fig. 4.

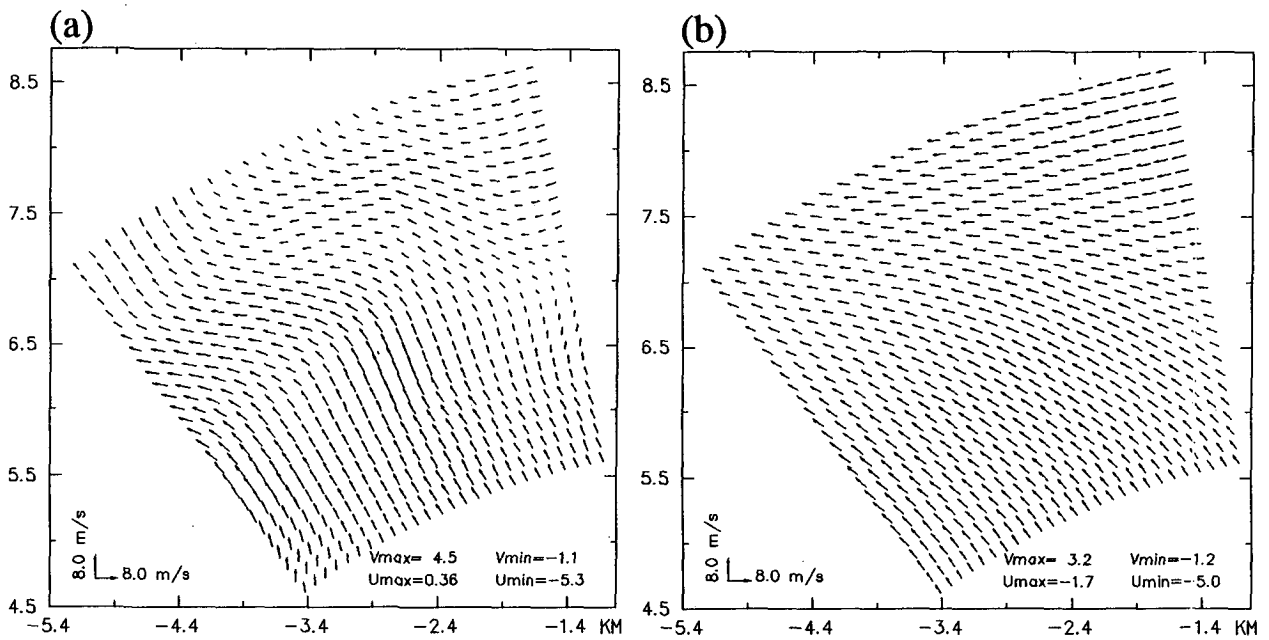

FIG. 2. Retrieved time-mean winds in experiment A3 for (a) method GSA and (b) method SSA. The statistics are listed in Table 3.

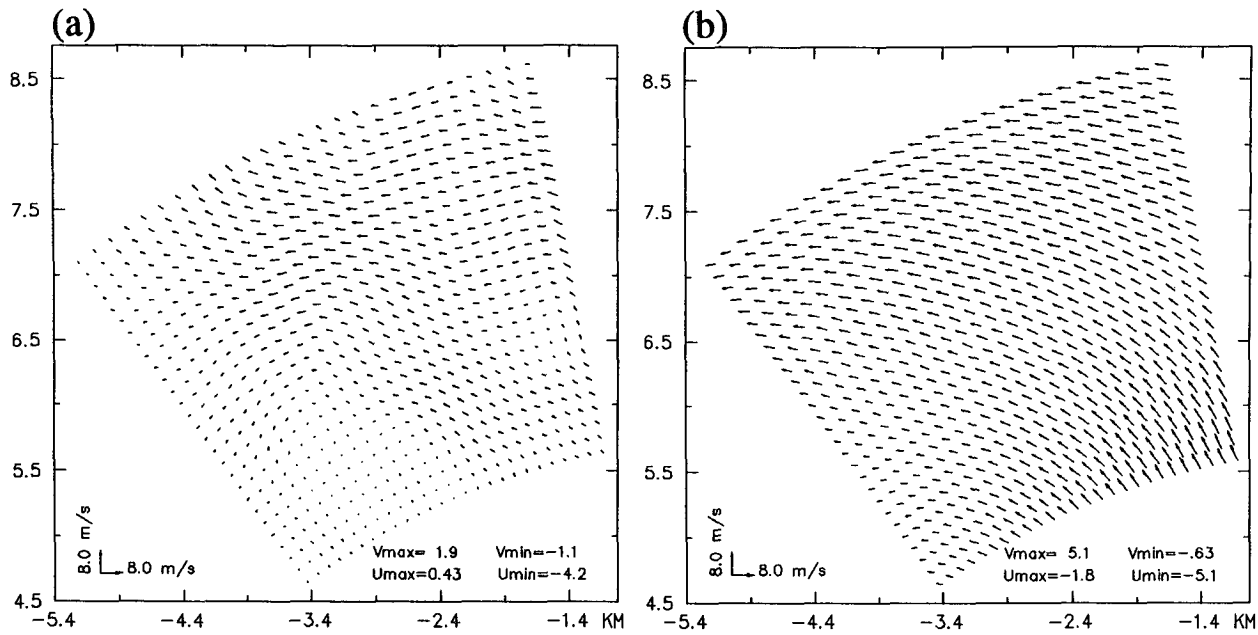

FIG. 3. Retrieved time-mean winds in experiment A4 for (a) method GSA and (b) method SSA. The statistics are listed in Table 4.

Note that the tracer field has zero gradient over the "plateau" and remains constant during the entire retrieving period ($\tau = 10\Delta\tau$), so the advection cannot be locally detected. On the other hand, the (truncated) SSA method detects only the long-wave components of the advection and each spectral component is global in the grid space, so the long-wave structures can be retrieved even though the tracer field contains a local region of zero gradient during the entire retrieving period. This is an extreme example showing the advantage of using the truncated spectral expression. Here, without showing the detailed result, it is necessary to point out that the SSA method will produce nearly the same results as the GSA method if the full spectral expansion ($M = 10$) is used.

The second example assumes that the "true" velocity field u contains only a short-wave mode, that is,

$$u = \sin(2k\pi x), \tag{4.6}$$

where $k = 8 > M = 5$. The initial and boundary conditions are the same as in (4.2), (4.3), and Fig. 4. Since the short-wave mode ($k = 8$) is not resolved by the truncated expansion (4.5) (with $M = 5$), there is no way for the SSA method to retrieve the short-wave mode. This is an extreme case showing the limitation of using the truncated spectral expression. As shown in Fig. 6, the SSA method fails completely, while the GSA method can still retrieve most of the grid values of u except for the "plateau." It appears that the SSA method "tends" to "force" its own short-wave mode

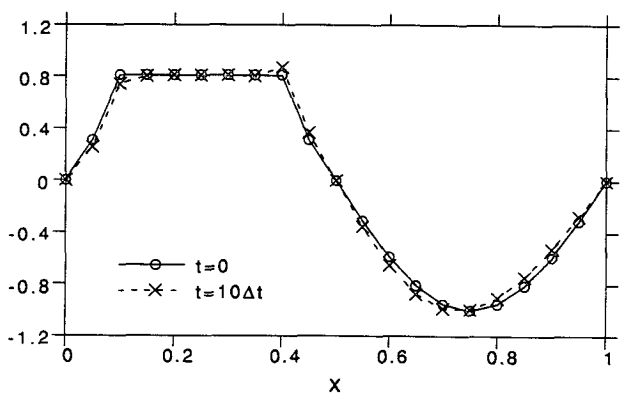

FIG. 4. Initial ($t = 0$) and final ($t = 10\Delta t$) tracer fields in the 1D experiment.

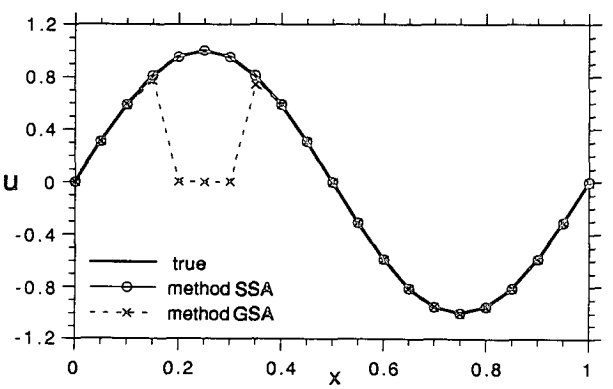

FIG. 5. True and retrieved u fields in 1D experiment with $k = 1$ in Eq. (4.6).

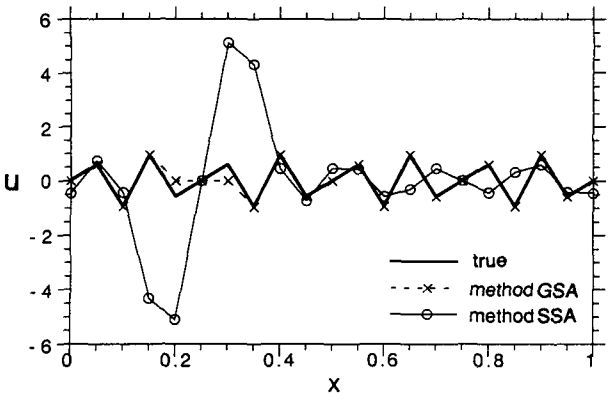

FIG. 6. As in Fig. 5 but with $k = 8$ in Eq. (4.6).

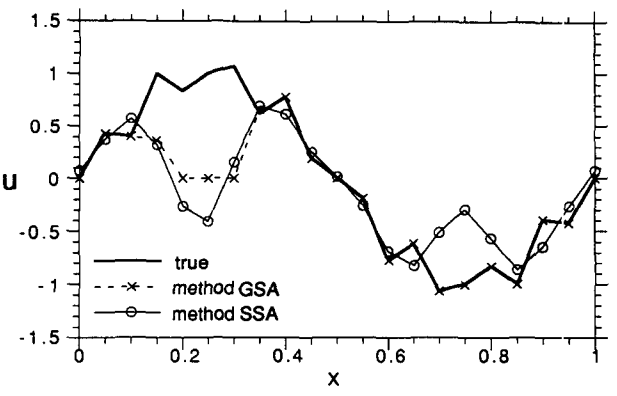

FIG. 7. As in Fig. 5 but with $a = 0.2$ and $k = 8$ in Eq. (4.7).

[$M = 5$ in the expansion (4.5)] to "fit" into the real short-wave mode ($k = 8$) in the velocity field, but the "misfit" errors are severe. The large amplitude error in the "plateau" region resembles the Gibbs effect, while the phase and wavelength errors in the remaining regions resemble the aliasing effect (Haltiner and Williams 1979).

The third example is a more realistic situation in which the "true" velocity field u contains both a long-wave mode and a short-wave mode, that is,

$$u = \sin(2\pi x) + a \sin(2k\pi x) \quad \text{with} \quad k = 8 > M = 5, \quad (4.7)$$

where a is the short-wave amplitude relative to the long wave. The initial and boundary conditions are the same as in (4.2), (4.3), and Fig. 4. Since the short-wave mode ($k = 8$) is not resolved by the truncated expansion, the relative superiority (or inferiority) of the SSA method to the GSA method is expected to depend on the smallness of a. This is indeed the case and, at least, we have already seen above two extreme cases for $a \to 0$ and $a \to \infty$. Experiments are performed with different values of a and the results show that the SSA method has a smaller (larger) rms error than the GSA method as $a < 0.15$ (or $a > 0.15$). A comparison of the two retrievals for $a = 0.2$ is shown in Fig. 7.

The fourth example uses the same data as in the above third example but the short wave is suppressed by the following three-grid smoothing:

$$\eta_i \leftarrow 0.25\eta_{i-1} + 0.5\eta_i + 0.25\eta_{i+1}. \quad (4.8)$$

This treatment may represent the effect of a relatively large Cressman radius as in section 3a and XQY94a,b. Although the original purpose of using a relatively large Cressman radius is to filter radar noise from observational data, here it is not necessary to add (artificial) radar noise to the data to simulate the real situation because our primary interest is to see how the two methods are affected by smoothing as in (4.8). As the short-wave signals in the tracer field (generated by the short mode of $k = 8$ in u) are largely filtered by (4.8), the performance of the SSA method is significantly improved as clearly seen from Fig. 8 in comparison with Fig. 7. A series of experiments is performed for different values of a and the results are summarized as follows:

(i) Using (4.8) improves the performance of the SSA method for nearly any finite a (except for $a \to 0$) and especially when a is large (although the retrieval itself becomes poor as a is large).

(ii) Using (4.8) slightly degrades the performance of the GSA method with idealized "perfect" data. When data contain short-wave radar noise, a proper short-wave filter can improve the GSA method (as shown in XQY94a,b).

(iii) If (4.8) is used in both methods, then the SSA method has smaller rms error than the GSA method for all finite a up to $a = 1$ or even larger. (Note that real data can be characterized by $a < 1$.)

(iv) If (4.8) is used only in the SSA method, then the SSA method has smaller (larger) rms error than the GSA method as $a < 0.5$ (or $a > 0.5$).

So far, we have seen that using idealized error-free data allows us to make clean comparisons between the

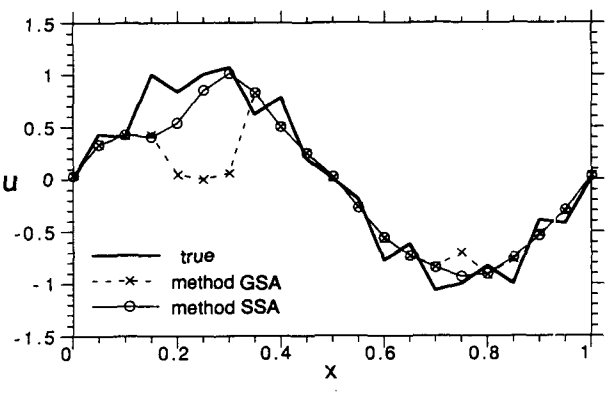

FIG. 8. As in Fig. 7 but the tracer data are smoothed.

SSA and GSA methods and to see their very basic merits and limitations. When the methods are applied to real data, such as the Phoenix II data, observational errors and radar noise should be properly filtered. In this case, the short-wave signals are also suppressed and, thus, points (i) and (iii) should be more relevant to practical applications than points (ii) and (iv). Based on points (i) and (iii), the SSA method with (4.8) has the smallest rms error, at least, for $a \leq 1$. However, this does not mean that the SSA method with (4.8) always has better performance. For example, if the initial tracer field has the same sinusoidal shape as in Fig. 1 of QX92 without the "plateau" and the velocity field contains only a short-wave mode as in the above second example, then the GSA method will produce a better retrieval than the SSA method with (4.8), simply because the SSA method cannot retrieve the short-wave mode and there is no persistent zero-gradient "plateau" region in the data field to hinder the GSA method.

5. Conclusions

In this paper, a spectral simple adjoint (SSA) method is developed based on the previous grid simple adjoint (GSA) method of XQY94b and tested with the Phoenix II field experimental data for retrieving low-altitude time-mean horizontal winds from single-Doppler wind data. The results show that when the excessive spatial resolution for the retrieved field in the GSA method is reduced by using a truncated spectral expression in the SSA method, the retrieval gains accuracy and/or temporal resolution (see Tables 1–4). A related important fact is that the time-mean wind fields were quite smooth in the Phoenix II case and, thus, the full grid resolution in the GSA method was unnecessary. In addition to this data property, the performance of the SSA method is also enhanced by the use of a relatively large Cressman radius that not only filters the radar noise but also suppresses (true) short-wave signals. Since the short-wave modes are not resolved by the truncated spectral expansion and their existence can only cause errors for the SSA method, suppressing (true) short-wave signals can improve the SSA method in retrieving the long-wave modes.

In terms of using a truncated expansion to optimally adjust the spatial resolution, the SSA method shares the same basic principle as the spectral variational method of Scialom and Lemaitre (1990). Actually, if we drop the dynamic constraints and retain only the kinematic constraints (mass continuity equation and rigid boundary condition at the ground level), then the SSA method reduces to the spectral variational method. In this sense, the SSA method is an extension of the spectral variational method, while the spectral variational method can be considered as an extension of the velocity–azimuth display (VAD) method (Browning and Wexler 1968) for single-Doppler data analyses. [The VAD method retrieves the vertical profiles of some mean features such as divergence and deformation (but not vorticity) averaged on each level of the scan volume from a single Doppler radar, while the spectral variational method retrieves the coefficients of a truncated spectral expression for the wind field.] Like the VAD method, the spectral variational method uses only the kinematic constraints (mass continuity equation and rigid boundary condition at the ground level) on a single time level, so the method cannot utilize the information implied by the observed movements of reflectivity patterns or/and radial wind patterns. Because of this, the spectral variational method may only retrieve coarse resolution winds from single-Doppler data. By incorporating the dynamic constraints (the radial momentum equation and/or reflectivity equation), the SSA method can use data over multiple time levels and, thus, significantly improve both the accuracy and the spatial resolution of the retrievals.

The basic merits and limitations for the SSA method are examined with idealized examples in comparison with the GSA method. It is shown that the GSA method cannot retrieve the velocity in regions where the tracer field has no gradient during the entire retrieving period, because the advection cannot be locally detected. On the other hand, the SSA method detects only the long-wave components of the advection and each spectral component is global in the grid space, so the long-wave structures can be retrieved even though the tracer field has zero gradient locally. The SSA method, however, cannot retrieve the short-wave modes. If the flow structure contains strong short-wave modes, then the SSA method will "force" its own (truncated) modes to "fit" into the short-wave modes and errors due to "misfit" can be severe (see Figs. 6–7). This is the worst scenario for the SSA method, although it can be improved (see Fig. 8) as the short-wave signals are suppressed by smoothing (which also filters radar noise in real data). In general, the SSA method will lose its advantage if the time-mean wind field is not smooth and needs to be resolved by nearly the same high resolution as the data.

Although only a limited number of experiments are presented and compared in this paper, the SSA method has been tested through a much larger number of experiments on different aspects of the method, similarly to those in XQY94a,b. Without showing the details, the main results are summarized as follows: (i) The basic merits of the original method of QX92 remain essential for the SSA method. (ii) The detailed treatments of data and selections of weights used in XQY94a remain significant for improving the retrieval. (iii) Retrieving the time-mean forcing (as in XQY94b) improves the retrieval significantly for both GSA and SSA methods.

Acknowledgments. The authors are thankful to Douglas K. Lilly, Tzvi Gal-Chen, Richard J. Doviak,

Hongdao Gu, Alan Shapiro, Shuowen Yang, Jin-Xiang Yu, Dušan Zrnić, and anonymous reviewers for their comments and suggestions. This work is supported by NOAA Contract NA90-RAH00078 at CIMMS and NSF Grant ATM-8809862 at CAPS, University of Oklahoma.

REFERENCES

Batchelor, G. K., 1967: *An Introduction to Fluid Dynamics.* Cambridge University Press, 615 pp.

Browning, K. A., and R. Wexler, 1968: The determination of kinematic properties of a wind field using Doppler radar. *J. Appl. Meteor.*, **7**, 105–113.

Chen, Q. S., and Y. H. Kuo, 1992: A harmonic-sine series expansion and its application to partitioning and reconstruction problems in a limited area. *Mon. Wea. Rev.*, **120**, 91–112.

Haltiner, G. J., and R. T. Williams, 1979: *Numerical Prediction and Dynamic Meteorology.* John Wiley & Sons, 477 pp.

Navon, I. M., X. Zou, J. Derber, and J. Sela, 1992: Variational data assimilation with an adiabatic version of the NMC spectral model. *Mon. Wea. Rev.*, **120**, 1433–1446.

Qiu, C. J., and Q. Xu, 1992: A simple adjoint method of wind analysis for single-Doppler data. *J. Atmos. Oceanic Technol.*, **9**, 588–598.

Sasaki, Y. K., 1970: Some basic formalisms in numerical variational analysis. *Mon. Wea. Rev.*, **98**, 875–883.

Schneider, J. M., and D. K. Lilly, 1986: PHOENIX II dual Doppler data analysis and preliminary results. Preprints, *Joint Sessions 23d Conf. on Radar Meteorology and Conf. on Cloud Physics,* Amer. Meteor. Soc., JP214–JP217.

Scialom, G., and Y. Lemaitre, 1990: A new analysis for the retrieval of three-dimensional mesoscale wind field from multiple Doppler radar. *J. Atmos. Oceanic Technol.*, **7**, 640–665.

Talagrand, O., and P. Courtier, 1987: Variational assimilation of meteorological observation with the adjoint vorticity equation. 1: Theory. *Quart. J. Roy. Meteor. Soc.*, **113**, 1311–1328.

Thacker, W. C., and R. B. Long, 1988: Fitting dynamics to data. *J. Geophys. Res.*, **93**, 1227–1240.

Xu, Q., and C. J. Qiu, 1994: Simple adjoint methods of single-Doppler wind analysis with a strong constraint of mass conservation. *J. Atmos. Oceanic Technol.*, **11**, 289–298.

——, ——, and J. X. Yu, 1992: An adjoint method for sea-surface currents from infrared images. *Sixth Conf. on Satellite Meteorology and Oceanography,* Atlanta, Amer. Meteor. Soc., 379–380.

——, ——, ——, J. X. Yu, H. D. Gu, and M. Wolfson, 1993: Adjoint-method retrievals of microburst winds from TDWR data. Preprints, *26th Int. Conf. on Radar Meteorology,* Norman, OK, Amer. Meteor. Soc., 433–434.

——, ——, and ——, 1994a: Adjoint-method retrievals of low-altitude wind fields from single-Doppler reflectivity measured during Phoenix II. *J. Atmos. Oceanic Technol.*, **11**, 275–288.

——, ——, and ——, 1994b: Adjoint-method retrievals of low-altitude wind fields from single-Doppler wind data. *J. Atmos. Oceanic Technol.*, **11**, 579–585.